ISSN 1330-3651(Print), ISSN 1848-6339 (Online)

https://doi.org/10.17559/TV-20250822002920
Original scientific paper

Dual-Surface Engineering of Fe_3O_4 Magnetic Nanoparticles: Enhanced Magnetorheological Performance and Tribological Mechanisms

Zhimin SUN, Feng REN*, Lan MEI

Abstract: Magnetic fluids are smart materials that fall under the category of magnetic materials and possess the property of fluidity. Nevertheless, conventional modifications using a monolayer surfactant are limited due to poor thermal stability and insufficient nanoparticle-carrier fluid compatibility. The synthesis of Fe_3O_4 nanoparticles via co-precipitation, is followed by a unique bilayer surface coating of oleic acid and boron-modified high molecular weight succinimide. The nanoparticles' characterization result indicates that as the nanoparticles were modified their diameter decreased from 13.66 nm to 11.39 nm. Their structure remained as cubic spinel structure with saturation magnetization of 61.48 emu/g. Analysis of FT-IR spectra confirmed that OA is anchored to the surface of the particles through the formation of Fe-OOC-R bonds. Hence, BSI will form a stable interfacial layer in this case. Rheological studies have shown a strong magnetoviscous effect in the magnetic field of 200 kA/m at 263 K which was suppressed when the temperature was raised to 313 K. According to tribological tests, the use of 4.5 wt% tungsten dialkyldithiocarbamate (WTDC) reduced friction, as the lowest CoF is indicated to occur at a value of *N* Load = 35 N at 6 Hz. Consequently, the technique presented herein will be used to create high-performance magnetic fluids for applications such as aerospace sealing and MEMS lubrication.

Keywords: co-precipitation method; dual-layer modification; Fe_3O_4 nanoparticles; magnetic fluid; magnetoviscous effect; tribological mechanisms; tribological performance

1 INTRODUCTION

Ferrofluids, or magnetic fluids, are stable colloidal suspensions of nanoscale magnetic particles dispersed in carrier liquids with surfactants. This exceptional combination of magnetic responsiveness and fluid properties makes them important smart materials [1]. According to Fig. 1, the system consists of three components. Superparamagnetic nanoparticles are tiny particles that exhibit magnetic behaviour but do not retain magnetism. Surface-active agents (e.g., oleic acid, dodecylbenzenesulfonic acid, or alkyl coupling agents) prevent nanoparticle agglomeration through chemical adsorption or steric hindrance [4]. The fluid's thermodynamic and rheological behavior is controlled by carrier liquids. These include synthetic hydrocarbons, silicone oil or ionic liquids. The surfactant usually has a polar head group that is attached to the surface of the nanoparticle, and a tail that is hydrophobic and compatible with the liquid carrier. Therefore, consequently, a double-layer structure is formed and stabilized [6]. The presence of an external magnetic field causes the magnetic nanoparticles to orient along the magnetic field lines, resulting in anisotropic viscosity and magnetostrictive behaviors as depicted in Fig. 1 [7]. The unique feature of ferrofluids made them usable in a wide range of applications like sealing, sensing, and energy conversion that are tough to replicate with conventional materials (Tab. 1).

The traditional methods of preparing ferrofluids have always been limited fundamentally by a single-layer surfactants coating. Incompatibility between surfactant and carrier liquid often causes the coating to desorb, resulting in particle sedimentation or phase separation [18]. The poorly thermodynamically stable nanoparticles with a single-layer coating are prone to phase separation on storage as they lack monodispersity [19]. The limited temperature tolerance is that surface surfactants can get carbonized at high temperatures (> 150 °C) whereas at low temperatures (< –20 °C) the viscosity of the carrier liquid increases rapidly resulting in particle aggregation [20]. Ferrofluid uses in harsh environments are greatly restricted due to these limitations.

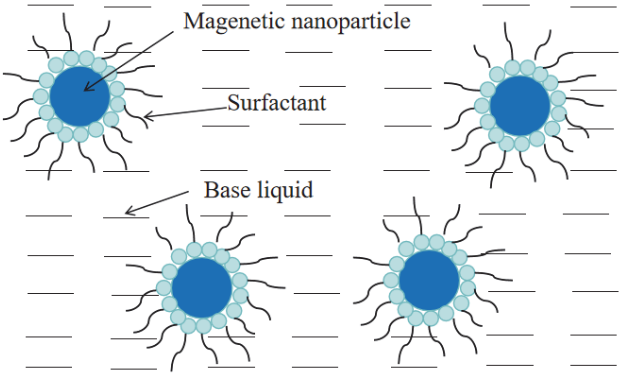

Figure 1 Compositions of magnetic fluids

The performance of a ferrofluid in modern industrial applications needs to be optimized in six ways. Aerospace sealing applications request for ferrofluids to retain their structural integrity above 200 °C and resist thermal decomposition of the surfactants for high-temperature stability [21]. In these polar areas, equipment at low-temperature levels requires that the fluid viscosity be maintained below 100 mPa·s at –50 °C level where the enhanced van der Waals force leads to nanoparticle agglomeration [22]. In the microelectromechanical systems (MEMS) actuation context, a high saturation magnetization (> 50 emu/g) and an ultra-fast response (< 10 ms) are required [23]. The ability of magneto-rheological systems to adjust their damping characteristics must be greater than four orders of magnitude if they are to be used for variable damping applications, such as smart shock absorbers. However, conventional systems suffer from shear failure at the particle-liquid interface. Long term stability should satisfy industrial criteria, such as sedimentation rates < 5% after one year, and a durability under 10^6 shear cycles in automotive suspensions [25, 26]. Lastly, for biomedical and electronic applications, environmental compatibility must comply with ISO 10993-5 biocompatibility standards and impede heavy metal emission [27].

Still many formulations fail to address weak nanoparticle-carrier adhesion. It is the major contributing reason for long-term instability, despite progress made so far using co-surfactant and interface engineering approaches. To address this problem, the current work proposes a double-layer surface modification using a bridging agent in the form of boronated high-molecular-weight succinimide (BSI). The long chain of BSI sometimes intertwines with synthetic hydrocarbons, forming a mechanism or coupling between the anchoring of the boron atoms of BSI with the OH groups on the surface of the Fe_3O_4 nanoparticles and the diffusion of the BSI in the synthetic hydrocarbon carriers. Following co-precipitation synthesis of Fe_3O_4 nanoparticles the oleic acid was used as a primary coating. BSI was then allowed to adsorb on the OA layer through its active -NH- groups to form strong molecular entanglements with the carrier liquid due to its high solubility. The resulting ferrofluid has greater saturation magnetization and more excellent thermal stability and anti-wear property than the traditional single-surfactant systems. The boron-based functionalization of BSI was critical to the strengthening of interfaces as well as the long-term colloidal stability. The researcher presents a promising route toward high-performance ferrofluids.

Table 1 Typical application of magnetic fluid

Medical/Industrial Application	Key Mechanism	Advantages	References
Vibration Damping	Energy dissipation through viscoelastic property modulation	Non-abrasive, energy-free operation, effective in low-frequency ranges	[8]
Sealing Technology	Formation of toroidal seals via magnetic fluid gap filling	Leak-proof performance, minimal wear, extended durability, simplified design	[9]
Environmental Remediation	Magnetic separation of pollutant-adsorbed particles	Rapid decontamination, reusability, eco-friendly processing	[10]
Sensing Systems	Magnetic field-dependent viscosity variation → pressure differential signal conversion	High sensitivity, noise immunity, linear response	[11]
Tribological Applications	Friction coefficient reduction via surfactant-mediated boundary lubrication	High load capacity, low acoustic emission, prolonged service life	[12]
Mineral Separation	Density-tunable ferrofluid-based density gradient separation	High-throughput sorting, adaptable operational parameters	[13]
Energy Harvesting	Magnetohydrodynamic power generation through field-driven flow	High efficiency, miniaturization potential, microsystem compatibility	[14]
Electronics Thermal Management	Eddy current-induced circulatory cooling	Moving part-free design, enhanced heat dissipation, IC chip applicability	[15]
Biomedical Engineering	Magnetic field-guided targeting combined with electromagnetic hyperthermia	Spatiotemporal precision, reduced off-target tissue damage	[16]
Smart Material Design	Field-responsive shape/mechanical property adaptation	Dynamic reconfigurability, biomimetic engineering feasibility	[17]

2 EXPERIMENTAL

2.1 Materials

All chemicals utilized in this investigation were analytically pure and applied without additional refinement. Comprehensive descriptions of the reagents, along with the experimental materials employed, are outlined in Tab 2.

Table 2 The chemicals used in the experiments

Compound Name	Chemical Formula	Purity	Supplier
Iron (III) chloride hexahydrate	$FeCl_3 \cdot 6H_2O$	97%	Sinopharm Chemical Reagent Co., Ltd., China
Iron (II) chloride tetrahydrate	$FeCl_2 \cdot 4H_2O$	98%	Sinopharm Chemical Reagent Co., Ltd., China
Ammonia aqueous solution	$NH_3 \cdot H_2O$	25%	Sinopharm Chemical Reagent Co., Ltd., China
cis-9-Octadecenoic acid	$C_{17}H_{33}COOH$	AR	Sinopharm Chemical Reagent Co., Ltd., China
Polyalphaolefin (PAO6)	$(C_nH_{2n})_x$	High Purity	CP-CHEM, USA
Acetone	C_3H_6O	AR	Sinopharm Chemical Reagent Co., Ltd., China
Succinimide	$C_4H_5NO_2$	99.5%	Jinzhou Jiarun Material Technology Co., Ltd., China
Tungsten Dialkyldithiocarbamate (WTDC)	W(S2CNR2)4	98%	Macklin, China

2.2 Preparation of Magnetic Fluid

2.2.1 Synthesis of Fe3O4 Nanoparticles by Coprecipitation

Fe_3O_4 nanoparticles were made using a chemical process. A Fe^{3+}/Fe^{2+} molar ratio of 2:1 was weighed (in grams) for $FeCl_3 \cdot 6H_2O$ (0.2 mol) and $FeCl_2 \cdot 4H_2O$ (0.1 mol). The blend was diluted with 300 mL of deionized water. The solution was stirred continuously at 400 rpm and maintained at 60 °C to accelerate the hydrolysis kinetics and reduce the local supersaturation that may produce agglomeration of particles. Afterward, dropwise addition of 100 mL of 25% ammonia solution to adjust the pH between 9.5-11 causes the coprecipitation of Fe^{2+} and Fe^{3+} ions 29. Ammonia is the precipitating agent, which offers additional OH^- that is helpful for the formation of colloids of iron (II) hydroxide and iron (III) hydroxide. These undergo Ostwald ripening to form nuclei of iron (II, III) oxide as per the following reaction: $Fe^{2+} + 2Fe^{3+} + 8OH^- \rightarrow Fe_3O_4\downarrow + 4H_2O$.

As the stirring was continued for another 30 minutes, the solution became increasingly black in nature which ensured crystallization and limitation of impurity phases like FeO or γ-Fe_2O_3. It was necessary to have strict control over Fe salt ratio, bath temperature, stirring speed and pH to achieve uniform Fe_3O_4 nanoparticles.

2.2.2 Oleic Acid Modification and Nanoparticle Purification

For surface modification and purification of the nanoparticle suspension during 1 hour, oleic acid of 10 mL was added and stirred. The pH was then fixed to neutral to overcome surface charge repulsion and help oleic acid molecules anchor on the particle surface thus optimizing colloidal stability [30]. The modified suspension was subjected to magnetic separation to magnetically collect superparamagnetic Fe_3O_4 particles by means of magnetic gradient force. The particles' washed three times with deionized water and acetone to remove unbound oleic acid and ionic impurities. It reduced their surface energy and minimized secondary aggregation upon drying. The cleaned particles were vacuum dried at 60 °C for 24 hours and subsequently ball milled to give oleic acid-coated Fe_3O_4 magnetic powder. The surface -OH groups of Fe_3O_4 chemically adsorb the carboxyl group of oleic acid forming Fe-OOC-R bonds. The long chain on the particle is hydrophobic, which creates steric hindrance to prevent agglomeration and ensures the completion of the coating process.

2.2.3 Preparation of Magnetic Fluid

To prepare and optimize the magnetic fluid, 10 mL of the boronated succinimide dispersant was first added to the polyalphaolefin based carrier liquid and stirred at 90 °C. After that, 20 g of modified Fe_3O_4 nanopowder was added, and the reaction was carried out at 150 °C for 2 hours. Mixture was left to magnetic sedimentation after reaction. The larger particles that were settled down in the bottom layer were removed and the uniform upper phase was collected as the final magnetic fluid.

The process comprised secondary surface modification and dispersion by BSI, high-temperature kinetic enhancement and magnetic separation by size. The polar functional groups of the BSI adsorbed onto the OA-coated nanoparticle surfaces, while its nonpolar chains were miscible in the PAO6 medium. The van der Waals attraction was reduced and long-term colloidal stability was enhanced. Through the increase in temperature (150 °C) BSI thermally moved over the surface which also leads to the uniform coverage of the surface by BSI and through the reduced viscosity of PAO6 it facilitates the wetting and dispersion of the nanoparticles. According to Stokes' law, larger particles with higher magnetic moments were allowed to sediment by magnetic sedimentation gauging, while particles smaller than 50 nm were retained in final fluid. This guaranteed high magnetic responsiveness and a low sedimentation rate.

2.3 Characterization of Magnetic Fluids

The synthesized magnetic particles were analyzed by X-ray diffraction (XRD), Fourier transform infrared spectroscopy (FT-IR), transmission electron microscopy (TEM), vibrating sample magnetometry (VSM) and rotational rheometry. For the XRD analysis, a Shimadzu XRD-7000 diffractometer with a Cu Kα radiation (λ = 0.15418 nm) was Article used at room temperature. To determine crystal structure and phase composition, scans were performed within a 2θ range of 20-80° at a rate of 2 °/min. FT-IR spectra were recorded with a PerkinElmer Spectrum Two spectrometer, range 4000-400 cm^{-1}, resolution 4 cm^{-1}, for functional groups and surface bonding characteristics identification. Jiangxi University of Science and Technology, China, was used to get the images. The study of the nanoparticle morphology and size distribution along with selected-area electron diffraction (SAED) was performed to confirm the lattice structure. We used Lake Shore 7407 Vibrating Sample Magnetometer at room temperature to measure magnetic properties. This study shows that hysteresis loops were recorded between –10000 to +10000 Oe to determine the saturation magnetization (Ms), coercivity (Hc) and remanence (Mr). The post Hysteresis Loops Recorded first appeared on Campus Chronicle.A rotational rheometer at 25 °C with TA Instruments AR2000ex Rheometer was used to analyse rheological properties. Dynamic frequency sweeps (0.1-100 Hz) and steady shear tests (shear rate: 0.1-1000 s^{-1}) were carried out to determine viscosity, storage modulus (G'), and loss modulus (G'') of the nanoparticle dispersions. The tribological performance of PAO6 base oil, Fe3O4-based magnetic fluids and nano-WTDC-enhanced magnetic fluids with 1.5% to 4.5% weight fractions were evaluated using the multi-functional friction tester (MS-M9000, Anton Paar, Austria). The counter samples which are made of 8-4 tin-based Babbitt alloy were 20 × 20 × 10 mm.

3 RESULTS AND DISCUSSION

3.1 XRD Analysis

The crystalline phases of Fe_3O_4 and oleic acid-modified Fe_3O_4 (OA@Fe_3O_4) were studied by X-ray diffraction (XRD) analysis. Fig. 2 shows the XRD patterns of Fe_3O_4 and OA@Fe_3O_4. The diffraction peaks of the pristine Fe3O4 sample show reflections characteristic of a cubic spinel structure. The most intense peaks are due to the (220), (311), (400), (422), (511) and (440) planes. The standard JCPDS card No. 19-0629 in good agreement confirms the phase-pure synthesis of Fe_3O_4. The (311) peak is very intense indicating the high crystallinity of the sample. The absence of any peak attributable to a secondary phase is also a good indication of the purity.

The average crystallite size was estimated by means of the Scherrer equation and found to be some 16.8 nm in size which is commonly seen in magnetic nanoparticles.

The positions of diffraction peaks namely for the OA@Fe_3O_4 sample remain the same and identical to Fe_3O_4 without coating. It means that the coating oleic acid on Fe_3O_4 has no influence on the origin cubic spinel structure. The highest intensities were much lower, possibly due to the layer of oléic acid being amorphous which absorbs or scatters some of the incident X-rays. The calculated crystallite size of OA@Fe_3O_4 was approximately 13.9 nm, suggesting that the oleic acid coating may inhibit crystal growth or induce surface defects, leading to a slight reduction in grain size.

The XRD results show that oleic acid was grafted on the surface of Fe_3O_4 nanoparticles without affecting its crystal phase. Surfactant covering nanoparticles produce a surface modifying amorphous layer with reduced peak intensity and slight refinement in size of crystallites. The absence of other diffraction peaks reveals that the modification process introduced no crystalline impurities, reaffirming that the samples possess high phase purity.

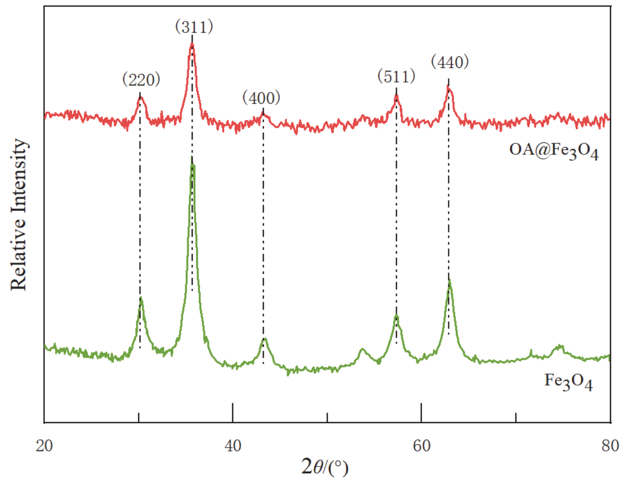

Figure 2 XRD patterns of Fe_3O_4 and OA@Fe_3O_4

3.2 IR

The FT-IR spectra of Fe_3O_4 and OA@Fe_3O_4 nanoparticles are displayed in Fig. 3. The wide absorption band found at 3244.2 cm^{-1} of Fe_3O_4 spectrum is due to the stretching vibrations of -OH molecular water or hydroxyl groups that implies the existence of moisture or surface hydroxyl on particles. A weak signal at 2236.6 cm^{-1} may correspond to a trace organic impurity, probably due to $C \equiv N$ or $C \equiv C$ vibrations. The peaks seen near 1013.8 cm^{-1} and 872.5 cm^{-1} are the signature of bending or lattice vibrations of the Fe-O-Fe species due to their spinel configuration of Fe_3O_4. The band at 768.1 cm^{-1} is probably due to Fe-O stretching vibrations but it seems somewhat strangely shifted from the normal Fe-O band (~ 579 cm^{-1}) seen in the literature. The causes behind this difference could be size effects of the nanoparticles or experimental conditions. The results indicate that the sample is highly pure and has a good crystal structure.

For the OA@Fe_3O_4 sample, the Fe-O related peak at 768.1 cm^{-1} shows a marked decrease in intensity, which may be attributed to the shielding effect of the oleic acid layer on surface vibrations. An additional vibration at 3362.5 cm^{-1} appears that corresponds to the -OH or -NH stretching vibrations of functional groups present on the oleic acid itself. The peak observed at 2277.5 cm^{-1} can be correlated to $C \equiv O$ or $C \equiv N$ functional groups resulting from incomplete reaction or a side product due to surface modification. The new absorption bands at 1550.8 cm^{-1} and 1345.6 cm^{-1} are attributed to the asymmetric and symmetric stretching vibrations of the carboxylate group ($-COO^-$), respectively, suggesting that oleic acid has a chemical bond with the Fe_3O_4 surface through its carboxyl. Furthermore, the peak at 941.1 cm^{-1} may be due to the formation of C-O-Fe bonds, providing further evidence for chemisorption. A weaker band at 467.2 cm^{-1} may arise from Fe-O lattice vibrations, which are probably caused by partial disruption of the degree of lattice due to surface modification.

Comparing the spectra of Fe_3O_4 and OA@Fe_3O_4, the decrease in Fe-O peak intensity (768.1 cm^{-1}) after oleic acid treatment confirms the coverage of active surface sites. The presence of the double peaks at 1550.8 cm^{-1} and 1345.6 cm^{-1} clearly indicates the formation of COO-Fe linkages due to chemical bonding between the carboxyl group of oleic acid and surface hydroxyl groups of Fe_3O_4. The stronger O-H group at 3362.5 cm^{-1} indicates the presence of hydrogen bonding between oleic acid. The peak at 2277.5 cm^{-1} may indicate unreacted functional groups or side-products, which can be substantiated with assistance from further characterization means.

In conclusion, Fe_3O_4 surface was effectively functionalized by oleic acid by means of chemisorption and encapsulation. This change made the spinel crystal the same while improving better organic-inorganic interfacial stability, which can lay a good foundation for the application of this ferrofluid in seals and other areas.

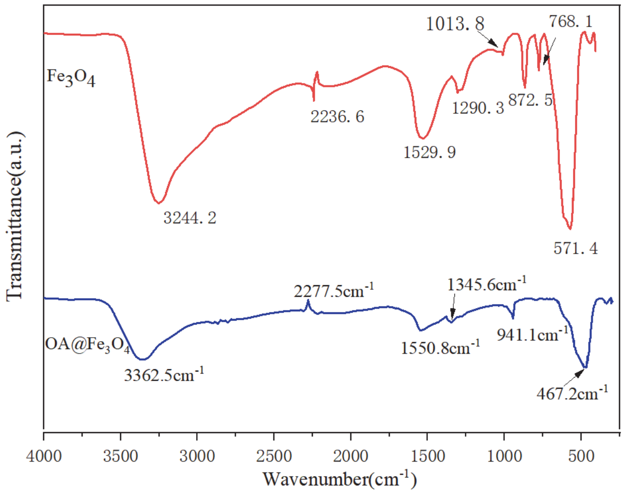

Figure 3 FT-IR spectra of Fe_3O_4 and OA@Fe_3O_4

3.3 TEM

The Fe_3O_4 nanoparticles displayed a quasi-spherical morphology with slight shape irregularities (Fig. 4a), indicating that the Ostwald ripening mechanism controlled their particle growth during coprecipitation. The particle size distribution was performed with measurements from 150 individual nanoparticles (Fig. 4b). The thus obtained particle size distribution shows a Gaussian profile with a mean size of 13.66 ± 0.26 nm and a size range of 8-20 nm. The relatively broad distribution indicates that the nucleation and growth stages were not well decoupled, suggesting that further synthesis optimization with respect to kinetic control is needed.

As per the LaMer model, the balance of nucleation rate (knucleation) and growth rate (kgrowth) is a crucial factor in particle monodispersity. When nucleation is less than growth, secondary growth dominates. This causes the particle size distributions to be much broader. In the present study coprecipitation of Fe^{3+} and Fe^{2+} probably involved local pH gradients which resulted in heterogeneous aggregation of $Fe(OH)_3$ and $Fe(OH)_2$ colloids increasing size heterogeneity.

Fig. 4c shows the TEM image of OA@Fe_3O_4 nanoparticles. They have a quasi-spherical structure with much higher size uniformity. The graph of Gaussian-fitted distribution (Fig. 4d) confirms that the produced particles have 11.39 ± 0.90 nm (average particle diameter) so they are comparatively lower and also have smaller size range (10-18 nm). The enhancement is due to the 2-channel effect of oleic acid (OA) on particle surface modification. The carboxyl groups of OA molecules firstly take a strong coordination bond with surface Fe^{3+} ions, which causes the molecules to chemically anchor to the nanoparticle surface and inhibits subsequent Ostwald ripening occurring during the crystal growth process, thus limiting the particle size formation. Secondly, the long, hydrophobic alkyl chains of OA are sterically hindered. As a result, these surfaces effectively reduce the van der Waals and magnetic dipole-dipole interactions between particles, which suppresses secondary agglomeration. The nanoparticles modified with OA show better dispersion and narrower size distribution due to this combined effect.

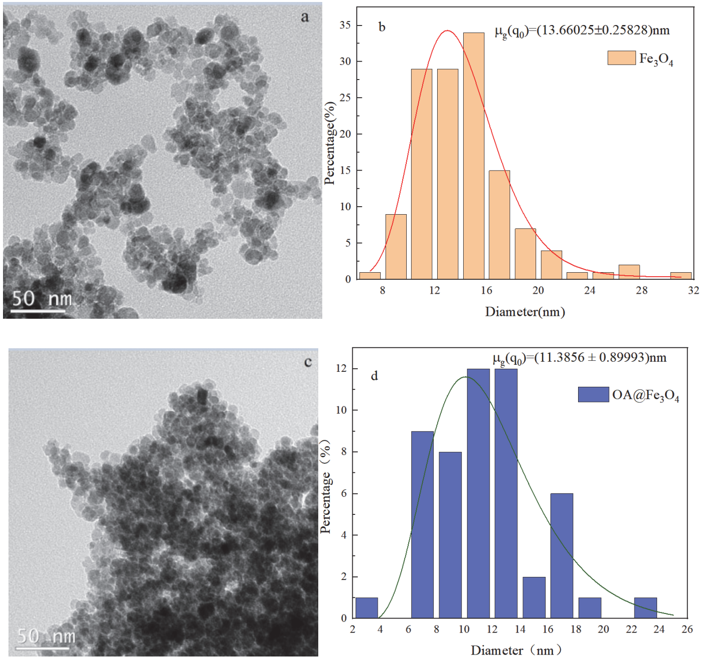

Figure 4 TEM images and size distribution histograms of Fe_3O_4 (a) and OA@Fe_3O_4 (b)

3.4 VSM

The magnetic characteristics of Fe_3O_4 and oleic acid (OA) modified Fe_3O_4 (OA@Fe_3O_4) were measured at 300 K by using a vibrating sample magnetometer (VSM) under an applied magnetic field of −10000 to +10000 Oe. The magnetization curves were shown in Fig. 5. The curves for both the samples show a typical S-type magnetization curve, which does not display hysteresis, remanence, or coercivity. The superparamagnetic features of the Fe_3O_4 nanoparticles were preserved during surface modification.

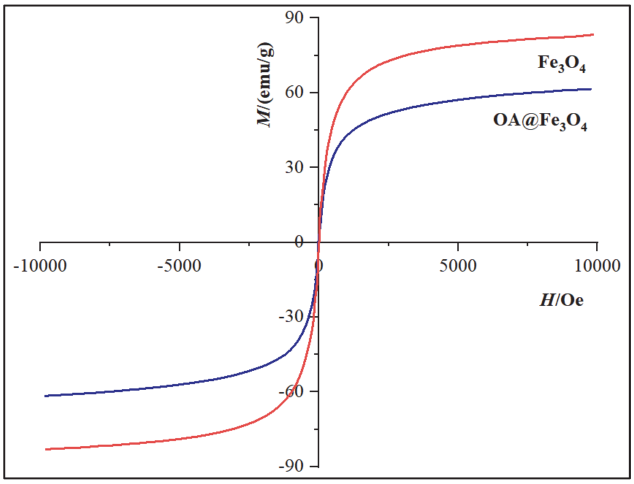

Figure 5 Magnetization curve of Fe_3O_4 and OA@Fe_3O_4

The exact value of saturation magnetization (*Ms*) for uncoated Fe_3O_4 nanoparticles was close to 83.27 emu/g, which is in close agreement with the reported value of high purity Fe_3O_4 [31]. This indicates the high crystallinity and strong magnetic ordering of synthesized particles. The observed superparamagnetic behaviour is a result of nanoparticles' nanoscale size: when the particle diameter is smaller than the critical single-domain limit, thermal energy can overcome energy barriers associated with magnetic anisotropy, leading to spontaneous reversal of the nanoparticles' magnetic moment. Hence, the macroscopic magnetization is of zero coercivity and remanence. The nanoparticles of the present invention have high magnetic response and single-domain character. This is supported by the quick saturation of the magnetic field at relatively low fields (±5000 Oe).

In the case of OA@Fe_3O_4, the magnetization curve retained its superparamagnetic shape, but the *Ms* value significantly decreased to 61.48 emu/g, representing a reduction of approximately 26.17%. Cathodic synthesis decreases during the electrochemical co-deposition of graphite because of some effects of non-magnetic oleic acid shell. To begin with, the organic coating creates a mass dilution effect which reduces the weight fraction of magnetic Fe_3O_4 per unit mass of the composite material. Additionally, due to the formation of surface –COO-Fe bonds between oleic acid and Fe_3O_4, spin canting or pinning may occur at the interface, disturbing the alignment of surface magnetic moments causing less net magnetization. Furthermore, the reduction in particle size, which is positively correlated to *Ms*, is responsible for the lower response observed [32].

The superparamagnetic characteristics of OA@Fe_3O_4, even with the reduction of *Ms*, suggested that the oleic acid modification did not interfere with the magnetic ordering of Fe_3O_4 core. Instead, the surface modification changed the global magnetic behaviour due to interfacial effects. The findings are in accordance with FT-IR which explains the chemical bonding features and the XRD results which maintain the crystal structure.

3.5 Magneto-Viscous Effect of the Magnetic Fluid

According to Fig. 6, all the magneto-viscosity curves show a strong thickening behaviour. In the low field region (H < 200 kA/m), viscosity increases sharply with the magnetic field. As the field strength moves into the high-field (200-600 kA/m) region, the rate of viscosity increase becomes increasingly slower and eventually approaches a saturation plateau. The changing microstructure of the ferrofluid induced by the field causes this nonlinear response. Under shear flow, magnetic nanoparticles tend to align into chain-like structures in the direction of the applied field. The way these chains align with the flow vorticity direction governs the degree of hydrodynamic resistance.

When low field strengths are applied chains of particles orient in random direction with an increase in magnetic field, the chains begin to align with the vorticity direction which increases the resistance to flow and viscosity shoot up. Once the field becomes critical (~ 200 kA/m), the chains get highly ordered and further structural rearrangement is restricted so that the increase in viscosity reaches a plateau. The size distribution function, g_n, also has an impact on the strength of the MV effect. In the presence of a steady magnetic field, an increase in shear rate induces a shift of g_n to shorter chains. The shorter chains add less to the stress tensor than longer ones, so the overall magneto-viscous effect falls with increasing shear rates.

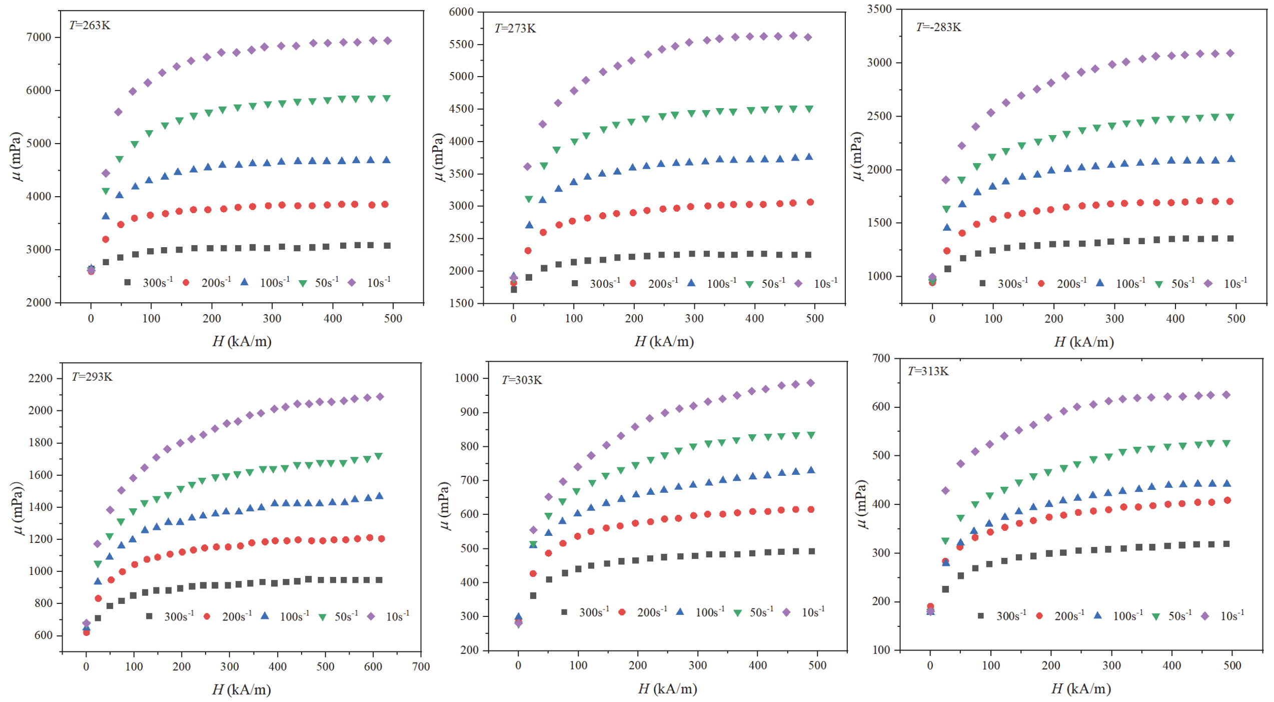

Figure 6 Magneto-viscous behavior of Fe_3O_4 ferrofluid under varying temperatures and magnetic fields

As shown in Fig. 6, the temperature-dependent magneto-viscosity behaviour of Fe_3O_4-based ferrofluid (263 K to 313 K). According to the data, temperature greatly influences the magneto-viscous response. The low-temperature region (263-283 K) has a viscosity that rises steeply with a field while the critical saturation field remains low (~ 200 kA/m). In comparison, at temperatures of 303-313 (K), the rate of increase of viscosity is considerably lower and saturation occurs at a higher value of magnetic field (~ 300 kA/m). The effects of temperature on this can be accounted for in terms of a combination of the thermally modulated chain model with techno thermo dynamic. At low temperatures the thermal motion is suppressed and magnetic dipole-dipole interactions dominate. This leads to the formation of stable, elongated chains, which align well under shear flow and increase flow resistance and viscosity significantly. At lower temperatures, the higher viscosity of the carrier fluid also contributes to more magneto-viscous response. At temperatures greater than 303 K, increased thermal motion counteracts the magnetic dipolar interaction and causes frequent breakage and formation of chains. As the amount of short chains increases, their diminished contribution to hydrodynamic resistance counterbalances the viscosity response. Furthermore, as the temperature rises, the inherent viscosity of the carrier fluid also decreases thus lessening the impact of the magnetic field on the flow behaviour. At near-critical temperatures (~ 313 K), thermal fluctuations effectively disrupt chain formation, and field-induced alignment becomes impossible, leading to a vanishing magneto-viscous effect. This strong dependence of *K* on temperature indicates competition between the magnetic anisotropy energy (*K*) and thermal energy (k_{BT}). At low temperatures, *K* takes over and stabilizes the set chains. In contrast, at high temperatures, thermal fluctuations suppress magnetic ordering, resulting in a weak magneto-viscous.

4 TRIBOTEST

4.1 Effect of WTDC Mass Fraction

Fig. 7 shows how the friction coefficients changed with time for different lubrication conditions. Fig. 8 shows the average friction coefficient of the magnetic fluid as the WTDC mass fraction increases. The experimental results indicate that pure magnetic fluids and the WTDC mixture have 40-60% lower friction coefficients than PAO6. This highlights the superior tribological properties of magnetic fluids as compared to standard oils. As per theory, this improvement occurs due to the distinct structure of the nanoparticles which produces stable boundary lubricating films during friction. These films prevent contact between two rough surfaces, thereby reducing friction and wear. Also, the rheological characteristics of the magnetic fluids reduce the viscous resistance during the shear which helps in reducing the energy dissipation. The addition of WTDC enhances lubrication performance due to its nanoscale dispersibility and its ability to interact synergistically with the magnetic fluid matrix. The addition of WTDC to the surface forms a protective layer at the friction interface which is dense. Also, it fills surface micro-defects and stabilizes the load. Most definitely, it reduces the local stresses.

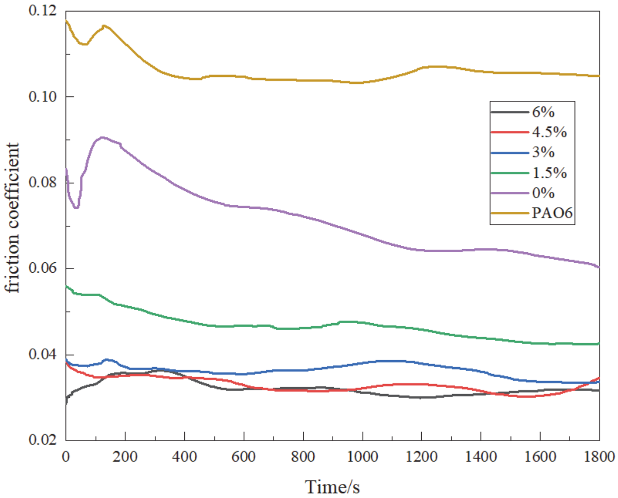

Figure 7 Changes of friction coefficient with time under different lubrication conditions

As the mass fraction of WTDC ranges from 0% to 4.5%, the friction coefficient lowers, indicating improved lubrication. This trend confirms the classical nano-additive lubrication theory of Zhang et al. (2020) that nanoparticles, through their rolling or sliding mechanisms, form a third-body layer to alleviate interfacial shear strength. When the WTDC concentration exceeds 4.5%, the agglomeration of nanoparticles leads to stabilization in the friction coefficient or a 5-8% rise. Localized agglomeration and uneven dispersion are caused by excessive concentrations. This compromises the continuity of the lubricant film. As a result, there is a higher chance of contact between friction pairs. Such aggregates could increase three-body abrasive wear which negates friction-reducing benefits.

It is known that the performance of magnetic fluid can be enhanced by WTDC. However, this only works effectively when the mass fraction is optimally controlled. According to experimental data, the ideal balance of film formation and disperse-ability of nanoparticles takes place at 4.5% WTDC. As a result, this magnetorheological fluid was used in later load and frequency tests.

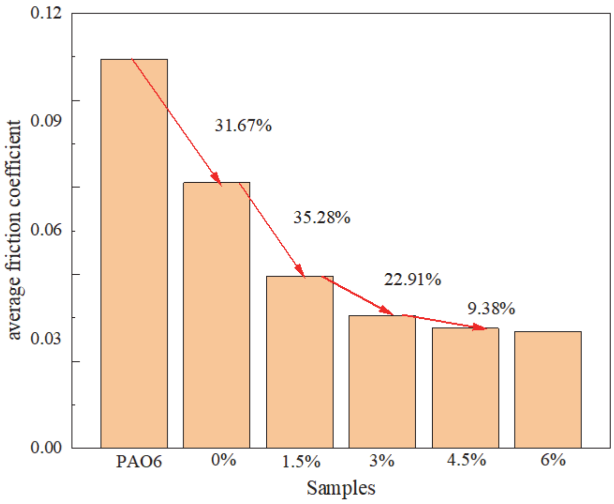

Figure 8 Changes of average friction coefficient with WTDC mass fraction

4.2 Effect of Normal Load

This study has systematically investigated the tribological performance of 4.5%-WTDC magnetic fluid at different normal loads (30-50 N). As observed from Fig. 9, the variation of the friction coefficient against time is shown and the correlation between the average friction coefficient and applied load is reported as per Fig. 10. It is seen that as the load is increased from 30 N to 35 N, the friction coefficient decreases but as it reaches beyond 40 N, it slowly increases, thus denoting its strong dependence on load.

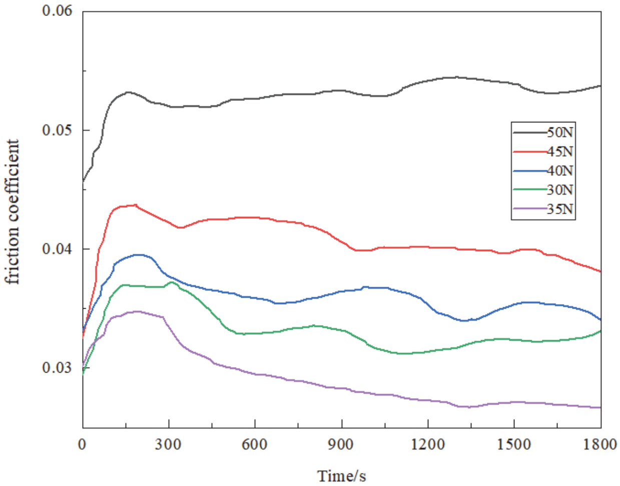

Figure 9 Changes of friction coefficient with time under different loads

The distribution of lubricant within an interfacial layer can explain the nonlinear variation pattern. The reduction in the coefficient of friction in the moderate load range (30-35 N) can be attributed to improved tribochemical reactions. When the contact pressure enhances, it promotes the thermal decomposition of tungsten dialkyldithiocarbamate (WTDC) present in the lubricant. This enhances the formation of tungsten disulfide (WS_2). This transition-metal sulfide orientates along the friction surface along a specific crystallographic plane to form a triboprotective film with low-shear-strength. Due to its interlayer sliding ability the friction resistance under boundary lubrication is greatly reduced.

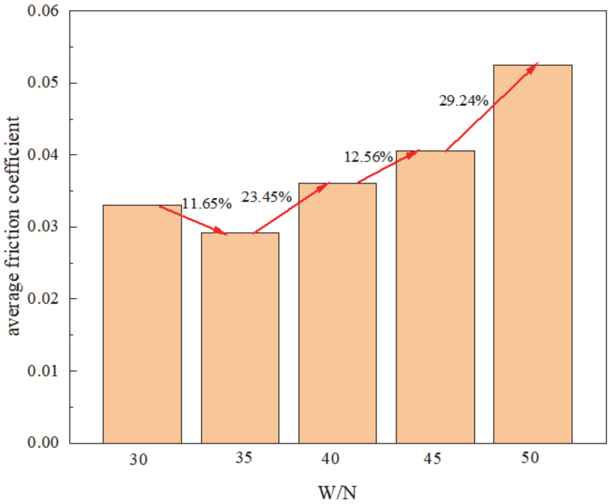

Figure 10 Changes of average friction coefficient with load

When the load fails to exceed the critical threshold (> 35 N), hydrodynamic effects starts to diminish while boundary lubrication becomes dominant, causing the friction coefficient to subsequently rise. There are three underlying mechanisms of this phenomenon. First, excessive mechanical loading (> 1.3 GPa) penetrates the lubricating film via surface asperities or sharp, rough points. Another possible form of evolution of the glance is for the combination of WS_2 to undergo plastic storage or even fracture under very great stresses with a steep rise in friction coefficient at 45 N as shown in Fig. Collapse of the lubricating film may occur because of 10. As per the Hertzian contact theory, the actual contact area is proportional to the square root of load. Hence, frictional energy dissipation increases at a super-linear rate with an increase in load. Additionally, nanoscale magnetic particles in the magnetic fluid may realign their magnetic domains when pressure is high. The resulting chain-like structures increase the rheological resistance, which is confirmed by the variable friction curve in the high loading area in Fig. 9.

4.3 Influence of Oscillation Frequency

Fig. 11 and Fig. 12 present the temporal evolution of the friction coefficient and its average over time for a magnetic fluid enhanced with 4.5% WTDC at frequencies 3-12 Hz. The findings show that the friction coefficient remained stable (fluctuation < 5%, 95% *CI*) in 3 to 6 Hz. The coefficient changed greatly after 6 Hz implying a nonlinear frequency-dependent tribology property.

Tribological analysis reveals that the low-frequency stability (3-6 Hz) originates from two adaptations:

(i) nanoparticles keeping the interfacial film intact at a low shear rate, and the conformational change of surface-adsorbed organic chains accommodating mechanical disturbance.

(ii) the anti-shear performance of the WS_2 tribofilm formed from the WTDC decomposition. This dissipates energy through the sliding of the crystallographic planes.

When the critical threshold of 6 Hz is exceeded, the system suddenly enters a high-friction state with a sudden increase in the coefficient. The mechanism involved is multiphysical coupling, wherein high-frequency sliding causes a rise in interface temperature (infrared thermography data). Through that, the lubricant degrades faster based on Arrhenius kinetics: $k = A_e^{(-E_a/RT)}$, herein, k denotes the Rate constant; A denotes the Pre-exponential factor; e denotes the Base of natural logarithm; E_a denotes the Activation energy; R denotes the Ideal gas constant; T denotes the Thermodynamic temperature which decreases viscosity and film-forming capacity. The increased dispersion of the data indicated in Fig. 12 after 9 Hz due to vibration caused the nanoparticles to agglomerate and the film to become non-homogeneous.

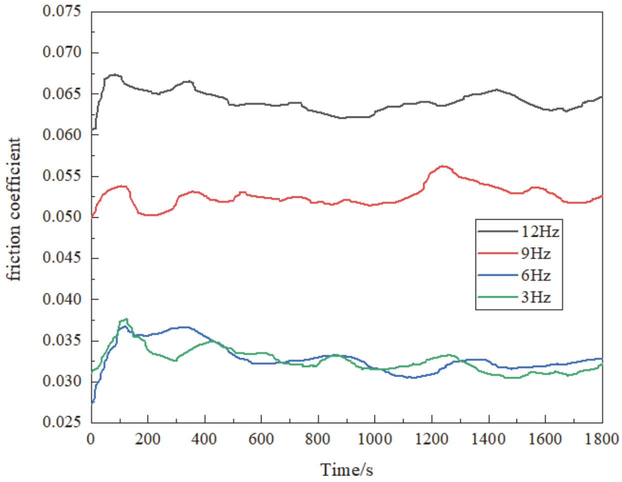

Figure 11 Changes of friction coefficient with time at different frequencies

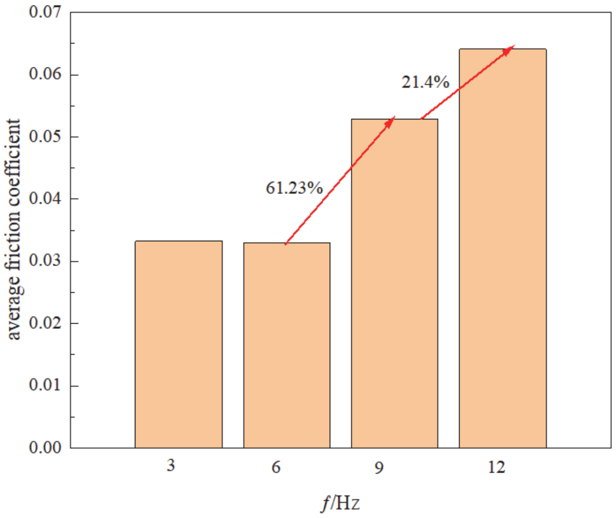

Figure 12 Changes of average friction coefficient with frequency

Tests revealed an optimal operation frequency ≤ 6 Hz for reciprocating. This data explains the frequency-effect mechanism: low frequency behavior is dependent on interfacial film stability and on thermo-mechanical coupling at high frequencies.

5 CONCLUSION

Fe_3O_4 magnetic nanoparticles were synthesized through co-precipitation in this study. Dual-layer surface modification using oleic acid (OA) and boronated high-molecular-weight succinimide (BSI) to create interfacial stability between nanoparticle and carrier liquid has been carried out successfully. The main conclusions are as follows.

(1) X-ray diffraction (XRD) and transmission electron microscopy results indicate that the cubic spinel structure of Fe_3O_4 was maintained on application of BSI/OA bilayer modification. It was also observed that the average particle size decreased from 13.66 nm to 11.39 nm with a strong increase in monodispersity. FT-IR analysis confirms the formation of Fe-OOC-R bonds between oleic acid and the Fe_3O_4 nanoparticles. Moreover, through the adsorption of polar groups and entanglement of alkyl chains, BSI can improve the interfacial stability between the nanoparticle and the base oil (PAO6).

(2) TheVSM test showed that after the modification of the material, it lost (61.48 emu/g) at a rate of 26.17%, which was due to the dilution by the organic shell. The nanoparticles were superparamagnetic and met the criteria that required a rapid magnetic response as well as applicability in MEMS devices. The magnetoviscous effect was significant at a temperature of 263 K but diminished at 313 K because thermal agitation was high. As a result, the formation of a chain-like structure was inhibited.

(3) The lubrication performance improvement was greatly enhanced by the introduction of WTDC. Application of WTDC at concentration of 4.5% was found to decrease from 0.13 to 0.08, which represents a fall of 40%. The WS_2 protective films not only enhanced the adsorption effects but also contributed to the rolling effect of the nanoparticles, leading to the observed improvement. Concentration too much made for a lumping effect so things became slippery. The WS_2 films retained its structure at a critical load of 35 N but breached the critical load when passed. The rupture of the film causes abrupt friction spikes. The lubricating film was stable at frequencies less than or equal to 6 Hz. However, degradation of lubricating film due to temperature as well as agglomeration of the lubricant increased the friction once the frequencies were above that.

This study establishes a foundation for the application of magnetic fluids in aerospace sealing, MEMS lubrication, and biomedical devices through the synergistic regulation of double-layer surface modification and lubrication additives. Future research may deepen investigations in four aspects: First, optimize extreme environment adaptability of the modification system by compounding novel modifiers or constructing composite structures to enhance stability and persistency of magnetic responsiveness under high temperature, high pressure, and strong magnetic fields. Second, deepen the understanding of the WTDC (water-based titanium-doped composite) mechanism by combining characterization and simulation to reveal interfacial bonding nature, while exploring synergistic effects with other nano-additives to suppress agglomeration. Third, advance functionalization for specific scenarios by studying lubrication mechanisms in microchannels for MEMS applications, and optimizing biocompatibility of modified layers for biomedical use. Fourth, refine the performance characterization system through in-situ techniques to track real-time structural evolution of lubricating films during friction processes, providing direct evidence for formulation optimization. These research directions are expected to achieve further breakthroughs in overcoming performance limitations of magnetic fluids and promote their practical engineering applications.

Acknowledgements

This work was partially supported by the Science and Technology Development Plan Project of Jilin Province, China (No. YDZJ202401597ZYTS), the Natural Science Foundation of Changchun Normal University (No. 2021010 and No. 2017007), and Jilin Province Development and Reform Commission, grant 2018C051-4.

6 REFERENCES

[1] Shliomis, M. I. (1974). Magnetic fluids. *Soviet Physics - Uspekhi*, *17*(2), 153-169. https://doi.org/10.1070/PU1974v017n02ABEH004332

[2] Selim, M. M., El-Safty, S., Tounsi, A., & Shenashen, M. (2023). Review of the impact of the external magnetic field on the characteristics of magnetic nanofluids. *Alexandria Engineering Journal*, *76*, 75-89. https://doi.org/10.1016/j.aej.2023.06.018

[3] Lemine, O. M., Algessair, S., Madkhali, N., Al-Najar, B., & El-Boubbou, K. (2023). Assessing the heat generation and self-heating mechanism of superparamagnetic Fe_3O_4 nanoparticles for magnetic hyperthermia application: The effects of concentration, frequency, and magnetic field. *Nanomaterials*, *13*(3), 13030453. https://doi.org/10.3390/nano13030453

[4] Li, L., Li, D., & Zhang, Z. (2022). Colloidal stability of magnetite nanoparticles coated by oleic acid and 3-(N, N-dimethylmyristylammonio)propanesulfonate in solvents. *Frontiers in Materials*, *9*, 893072. https://doi.org/10.3389/fmats.2022.893072

[5] Oehlsen, O., Cervantes-Ramírez, S. I., Cervantes-Avilés, P., & Medina-Veloz, I. A. (2022). Approaches on ferrofluid synthesis and applications: Current status and future perspectives. *ACS Omega*, *7*, 3134-3150. https://doi.org/10.1021/acsomega.1c05631

[6] Xu, F., Cao, Y., Gong, H., Li, J., Xu, Y., & Shi, L. (2024). Mass transport and energy conversion of magnetic nanofluids from nanoparticles' movement and liquid manipulation. *Processes*, *12*(5), 12050955. https://doi.org/10.3390/pr12050955

[7] Kredentser, S. V., Kalyk, M. M., Kalita, V. M., Slyusarenko, K. V., Reshetnyak, V. Yu., & Reznikov, Yu. A. (2017). Magneto-induced anisotropy in magnetic colloids of superparamagnetic nanoparticles in an external magnetic field. *Soft Matter*, *13*, 4080-4087. https://doi.org/10.1039/C7SM00795G

[8] Wang, J., Liu, Y. F., Qin, Z., Ma, L., & Chu, F. (2022). Dynamic performance of a novel integral magnetorheological damper-rotor system. *Mechanical Systems and Signal Processing*, *172*, 109004. https://doi.org/10.1016/j.ymssp.2022.109004

[9] Li, S., Xiu, S., Song, W., Sun, C., & Yang, H. (2023). Research on the wear characteristics of magnetorheological

fluid in sealing interface considering the interaction between surface roughness and magneticparticles. Tribology International, 185, 108496. https://doi.org/10.1016/j.triboint.2023.108496

[10] Ma, H., Pu, S., Hou, Y., Zhu, R., Zinchenko, A., & Chu, W. (2018). A highly efficient magnetic chitosan "fluid" adsorbent with a high capacity and fast adsorption kinetics for dyeing waste waterpurification. *Chemical Engineering Journa*l, *345*, 556-565. https://doi.org/10.1016/j.cej.2018.03.115

[11] Nature Editorial. (2024). A magnetic liquid makes for an injectable sensor in living tissue. *Nature*. https://doi.org/10.1038/d41586-024-01262-7

[12] Nie, S., Gong, F., Ji, H., Wang, Y., Che, C., & Zhang, G. (2024). Effect of surface texture on friction alenergy dissipation under magnetic fluid lubrication used for semi-active nonlinear energy sink. *Tribology International*, *192*, 109283. https://doi.org/10.1016/j.triboint.2024.109283

[13] Kang, Y. & Zhou, X. K. (2022). Research on remote control using magnetic fluid power generation. *Highlights in Science Engineering and Technology*, *7*, 26-30. https://doi.org/10.54097/hset.v7i.991

[14] Seol, M.-L., Jeon, S., Han, J.-W., & Choi, Y.-K. (2017). Ferrofluid-based triboelectric-electromagnetic hybrid generator for sensitive and sustainable vibration energy harvesting. *Nano Energy*, *31*, 233-238. https://doi.org/10.1016/j.nanoen.2016.11.038

[15] Pattanaik, M. S., Varma, V. B., Cheekati, S. K., Chaudhary, V., & Ramanujan, R. V. (2021). Optimal ferrofluids for magnetic cooling devices. ScientificReports, 11, 2467. https://doi.org/10.1038/s41598-021-03514-2

[16] Ji, Y., Bai, X., Sun, H., Wang, L., Gan, C., Jia, L., Xu, J., Zhang, W., Wang, Q., Yang, X., Hou, Y., Wang, Y., Hui, H., & Li, F. (2024). Biocompatible ferrofluid-based millirobot for tumor photothermal therapy in near-infrared-II window. *Advanced Healthcare Materials*, *13*, 2470027. https://doi.org/10.1002/adhm.202470027

[17] Zhang, X., Hou, K., Long, Y., & Song, K. (2024). Bioinspired intelligen tferrofluid: Old magnetic material with new optical properties. *Nano Letters*, *24*, 11559-11566. https://doi.org/10.1021/acs.nanolett.4c03083

[18] Streubel, R., Liu, K., Wu, X., & Russell, T. P. (2020). Perspective: Ferromagnetic liquids. *Materials*, *13*, 122712. https://doi.org/10.3390/ma13122712

[19] Xu, B., Luo, Y., & Ren, H. (2014). Review on magneto-rheological fluid and its application. *American Journal of Nanoscience and Nanotechnology*, *2*, 70-74. https://doi.org/10.11648/j.nano.20140204.12

[20] Ryapolov, P. A., Vasilyeva, A., Kalyuzhnaya, D., Churaev, A. A., Sokolov, E. A., & Shel'deshova, E. V. (2024). Magneticfluids: The interaction between the microstructure, macroscopic properties, and dynamics under different combinations of external influences. *Nanomaterials*, *14*(2), 14020222. https://doi.org/10.3390/nano14020222

[21] Ji, J., Wu, X., Tian, Z., Xie, F., Chen, F., & Li, H. (2023). A novel magnetorheological fluid with high-temperature resistance. *Materials*, *16*, 4207. https://doi.org/10.3390/ma16124207

[22] Sakamoto, H. (2021). Current status and prospects of new magnetorheological materials development. *Journal of the Japan Society of Applied Electromagnetics and Mechanics*, *29*, 635-642. https://doi.org/10.14243/jsaem.29.635

[23] Lu, Q., Choi, K., Nam, J.-D., & Choi, H. J. (2021). Magnetic polymer composite particles: Design and magnetorheology. *Polymers*, *13*, 13040512. https://doi.org/10.3390/polym13040512

[24] Zhang, Z., Li, D., Yu, M., Niu, X., & Li, W. (2023). Characterization and application of magneto-sensitive soft materials. *Frontiers in Materials*, *10*, 1210416. https://doi.org/10.3389/fmats.2023.1210416

[25] Radionov, A. V., Podoltsev, A. D., & Radionova, A. A. (2017). Express-method for determining the quality of a magnetic fluid for operation in the working gap of a magnetic fluid seal. *IOP Conference Series: Materials Science and Engineering*, *233*, 012038. https://doi.org/10.1088/1757-899X/233/1/012038

[26] Desrosiers, J.-F., LuckingBigué, J.-P., Denninger, M., Julió, G., Plante, J.-S., & Charron, F. (2013). Preliminary investigation of magneto-rheological fluid durability in continuous slippage clutch. *Journal of Physics*: *Conference Series*, *412*, 012022. https://doi.org/10.1088/1742-6596/412/1/012022

[27] Imran, M., Chaudhary, A. A., Ahmed, S., Alam, M. M., Khan, A., Zouli, N., Hakami, J., Rudayni, H. A., & Khan, S.-U.-D. (2022). Iron oxide nanoparticle-based ferro-nanofluids for advanced technological applications. *Molecules*, *27*, 27227931. https://doi.org/10.3390/molecules27227931

[28] Chen, N., Li, D., & Nie, S. (2024). Theoretical and experimental study on the preparation of high-viscosity magnetic nanofluid by combined surfactants. *ACS Omega*, *9*, 33522-33527. https://doi.org/10.1021/acsomega.4c01060

[29] Wang, Y., Wang, N., Wang, P., Yang, F., Han, C., & Yu, D. (2024). Preparation of magnetic dialdehyde starch-immobilized phospholipase A_1 and acyl transfer in reflection. International *Journal of Biological Macromolecules*, *257*, 128804. https://doi.org/10.1016/j.ijbiomac.2023.128804

[30] Jia, X., Liu, Z., Li, Q., Wang, Y., Shah, T., Ahmad, M., Zhang, Q., & Zhang, B. (2021). Wrinkled Fe_3O_4@C magneticcomposite microspheres: Regulation of magnetic content and their microwave absorbing performance. *Journal of Colloid and Interface Science*, *601*, 397-410. https://doi.org/10.1016/j.jcis.2021.05.153

[31] Rahmayanti, M., Santosa, S. J., & Sutarno. (2020). Modified humic acid from peat soils with magnetite (HA-Fe_3O_4) by using sonochemical technology for gold recovery. *Jurnal Bahan Alam Terbarukan*, *9*(2), 81-87. https://doi.org/10.15294/jbat.v9i02.26131

[32] Liu, J.-M., Wei, S.-Y., Liu, H.-L., Fang, G.-Z., & Wang, S. (2017). Preparation and evaluation of core-shell magnetic molecularly imprinted polymers for solid-phase extraction and determination of sterigmatocystin in food. *Polymers*, *9*(10), 546. https://doi.org/10.3390/polym9100546

Contact information:

Zhimin SUN
School of Engineering,
Changchun Normal University, Changchun, China

Feng REN
(Corresponding author)
School of Engineering,
Changchun Normal University, Changchun, China
E-mail: renfeng@ccsfu.edu.cn

Lan MEI
School of Chemistry,
Changchun Normal University, Changchun, China